Journal of Materials Chemistry A

ROYAL SOCIETY OF CHEMISTRY

PAPER

View Article Online
View Journal | View Issue

Cite this: J. Mater. Chem. A, 2024, 12, 13391

A comprehensive investigation of $Ag_7P_3X_{11}$ (X = {O, S, and Se}) solid-state silver superionic conductors†

Amin Niksirat, [a] Maryam Soleimani, [a] Ali Lashani Zand [a] and Mahdi Pourfath *[ab]

This study carefully analyzes and proposes a new class of high-performance inorganic solid-state electrolytes with the composition $Ag_7P_3X_{11}$ (X = {O, S, and Se}), using *ab initio* calculations. The structural and electronic properties, as well as electrochemical stability, were evaluated and discussed. Ionic conductivity of Ag^+ was determined through *ab initio* molecular dynamics simulations at various temperatures. The results indicate that the room-temperature ionic conductivity of $Ag_7P_3Se_{11}$ is approximately 13.98 mS cm^{-1}, which is higher than that of most other solid-state electrolytes. The calculated activation energy is relatively low at 0.197 eV. The phenomenon of Ag^+ ion transport was systematically studied by analyzing the diffusion minimum-energy pathways using the nudged elastic band (NEB) method. The electronic band gaps of the materials studied, calculated using the HSE06 method, ranged from 1.47 to 2.34 eV. Finally, the feasibility of synthesizing these proposed superionic materials was explored through phase stability calculations, including phonon analysis based on density functional perturbation theory (DFPT), thermodynamic stability, radial distribution function, and Gibbs free energy calculations. The results presented provide a guide for designing stable and safe superionic conductors.

Received 27th February 2024
Accepted 27th April 2024

DOI: 10.1039/d4ta01341g

rsc.li/materials-a

1 Introduction

The accelerated adoption of electric vehicles, mobile electronic and communication devices, and the transition to renewable energy sources have spurred the development of more energy-dense, safe, and cost-effective batteries.[1–3] Lithium-ion batteries (LIBs) are favored for their high power and energy density.[4–6] Although LIBs with liquid electrolytes provide excellent wetting capabilities and high conductivity,[7] they suffer from several drawbacks, including low ion selectivity, inadequate stability, and safety concerns.[8] Solid-state electrolytes (SSEs) address these issues,[9–11] enhancing safety, electrochemical and thermal stability, energy/power densities, and reducing packaging needs.[12–14]

SSEs are generally categorized into inorganic ceramic electrolytes and organic polymeric electrolytes.[15–17] An ideal SSE exhibits high ionic conductivity at room temperature, minimal activation barriers for ion diffusion, limited electronic conductivity, and maintains chemical and electrochemical stability at interfaces with the anode and cathode throughout cycling.[18] Extensive research has been conducted on new solid electrolytes such as $Li_{10}GeP_2S_{12}$,[19] $Li_7P_3S_{11}$,[20] $Li_7La_3Zr_2O_{12}$,[21,22] and $Li_{1+2x}Zn_{1-x}PS_4$.[23] Inorganic ceramic electrolytes typically include oxides[24] and sulfides,[25] with sulfide-based electrolytes like $Li_7P_3S_{11}$ offering high ionic conductivities at room temperature and mechanical properties comparable to traditional liquid electrolytes.[26–28]

Silver, easily recyclable and thus cost-effective and less resource-intensive,[29] exhibits superior chemical stability and temperature sensitivity compared to lithium, making it ideal for battery applications in military and aerospace sectors where higher safety standards are crucial.[30,31] The polarizable electron shells and ionic radius of silver facilitate its use as a fast ion medium.[32] In this study, inspired by the known sulfide-based superionic conductor $Li_7P_3S_{11}$,[33] a new class of silver superionic conductors, $Ag_7P_3X_{11}$ (X = {O, S, Se}), was explored. Using density functional theory (DFT) and *ab initio* molecular dynamics simulations (AIMD), the structural and electronic properties, diffusivity, and ion conductivity of $Ag_7P_3X_{11}$ were analyzed.

[a]School of Electrical and Computer Engineering, College of Engineering, University of Tehran, Tehran 14395-515, Iran. E-mail: pourfath@iue.tuwien.ac.at; pourfath@ut.ac.ir

[b]Institute for Microelectronics, TU Wien, Gusshausstrasse 27–29, A-1040 Vienna, Austria

† Electronic supplementary information (ESI) available: Thermal stability at 300 K has been assessed for $Ag_7P_3X_{11}$ structures with (X = {O, S and Se}), along with possible decomposition reactions and their corresponding energies. The radial distribution function (RDF), which measures the density $g(r)$ of finding an atom at a distance from a reference point, was analyzed for $Ag_7P_3X_{11}$ under various temperatures (600 K, 750 K, 900 K, and 1200 K). Structural snapshots from *ab initio* molecular dynamics (AIMD) simulations depict Ag^+ ion diffusion at 1200 K. Additionally, the nudged elastic band (NEB) method was used to graph the transport of Ag ions between two P_2S_7 pyrothiophosphate units across a narrow interstitial gap. See DOI: https://doi.org/10.1039/d4ta01341g

2 Approach

Ab initio molecular dynamics (AIMD) and density functional theory (DFT) calculations, as implemented in the Vienna *Ab Initio* Simulation Package (VASP),[34] were utilized in this study. The projector augmented wave method (PAW) was employed within the Perdew–Burke–Ernzerhof (PBE) form of the generalized gradient approximation (GGA) for structural relaxation,[35,36] with a 12 × 6 × 6 *k*-point grid and a kinetic energy cutoff of 400 eV for sulfides and selenides, and 500 eV for oxides.[37] Structural relaxations were carried out until the residual forces and energy differences were smaller than 0.01 eV $Å^{-1}$ and 10^{-6} eV, respectively.

The structural data for $Ag_7P_3X_{11}$ were obtained from the Materials Project database.[38] For the electronic property calculations, the triclinic crystal structure with the space group *P*1 was employed. All atoms were relaxed until the structure reached minimum energy, allowing the shape and volume of the supercell and the positions of the atoms to freely change until the convergence criteria were satisfied. The Heyd–Scuseria–Ernzerhof (HSE06) hybrid functional was also used to accurately evaluate the electronic properties.[39]

To gain insights into the interactions between Ag ions and anions in $Ag_7P_3X_{11}$ (X = {O, S, and Se}) and to assess the extent of charge transfer between these species, Bader charge calculations were utilized.[40,41] The nudged elastic band method (NEB) was employed to find the minimum-energy path for Ag^+ ion migration[42,43] in a large supercell comprising 2 × 2 × 1 unit cells to minimize interactions between periodic images.

AIMD simulations with the canonical ensemble (NVT) within the framework of DFT were performed to investigate diffusivity and conductivity.[44,45] A relaxed 2 × 2 × 1 supercell, expanding the 64-atom triclinic unit cell to a total of 246 atoms, was utilized.[46] The total AIMD simulation time was 45 ps with a time step of 2 fs, with the first 5 ps designated as equilibration time and therefore not included in the calculations.[47] The temperature was controlled using a Nose–Hoover thermostat,[48–51] starting at 100 K and subsequently increasing to 600 K, 750 K, 900 K, and 1200 K.[52] Throughout the AIMD simulations, the trajectories of all silver ions were monitored, and the total mean squared displacement (TMSD) of silver ions was calculated for each time interval Δt using the following equation:

$$\mathrm{TMSD}(\Delta t) = \sum_{i=1}^{N} \frac{1}{N_{\Delta t}} \sum_{t=0}^{t_{\mathrm{tot}}-\Delta t} |r_i(t+\Delta t) - r_i(t)|^2 \quad (1)$$

where r_i is the trajectory of silver ion i, $N_{\Delta t}$ is the total number of time intervals Δt during the entire duration t_{tot} of the AIMD simulation. The diffusivity of the ions can be determined using the Einstein relation:

$$D = \frac{1}{N} \frac{\mathrm{TMSD}(\Delta t)}{2d\Delta t} \quad (2)$$

where N is the number of diffusing atoms, and d is the number of diffusion dimensions. If the atomic displacement is remarkably larger than the vibration amplitude, this approach yields reliable values for tracer diffusivity.[53] Tracer diffusivity is only an approximation of ionic diffusion, but considering ion correlations and the center of mass displacement can lead to more accurate results.[53] As ion hopping is a stochastic process, the statistical deviations of the diffusivities were evaluated based on the mean squared displacement (MSD).[54] By using the diffusivity data and the Nernst–Einstein relation, assuming the Haven ratio is equal to one, the ionic conductivity (σ) can be approximated by:[53,55–57]

$$\sigma = \frac{ne^2z^2}{k_{\mathrm{B}}T} D \quad (3)$$

where n is the diffusing particle density, e is the elementary electron charge, z is the ionic charge, k_{B} is Boltzmann's constant, and T is the sample temperature in kelvin. The diffusion coefficient in solids at different temperatures is generally well predicted by the Arrhenius relation:[56,58]

$$D = D_0 \exp(-E_{\mathrm{a}}/(k_{\mathrm{B}}T)) \quad (4)$$

where D is the maximal diffusion coefficient (at infinite temperature), and E_{a} is the activation energy, assumed to be equal to the potential energy barrier before the ions start to diffuse.[59]

The atomic environment determines the forces and energy barriers that govern the behavior of diffusing atoms. The radial distribution function (RDF) is instrumental in revealing the density (g) of an element *versus* the distance (r) from another element during AIMD simulations:

$$g(r) = \frac{1}{n_{\mathrm{tot}}A} \sum_{x=1}^{A} \sum_{y=1}^{B} \sum_{n=1}^{n_{\mathrm{tot}}} g\left(r_{xy}(n)\right) \quad (5)$$

where A is the number of reference atoms for the RDF, B is the number of atoms of the other elements, n_{tot} is the total number of simulation time steps, and $r_{xy}(n)$ is the distance between atom x and y at some time step n. Given the positions of all atoms are available at every time steps of the AIMD simulation, RDFs can be readily obtained for any atomic site or element.[60]

Thermodynamic stability was assessed by calculating the total energy of phases based on DFT calculations. The stability of any phase was investigated by comparing its energy with the linear combinations of the energies of other phases using the convex hull construction. All compounds listed in the Inorganic Crystal Structure Database (ICSD) and other similar systems were considered.[61] The stability was quantified by the energy above the hull, which is always non-negative and indicates the magnitude of a compound's decomposition energy.[27]

Density functional perturbation theory (DFPT) is a powerful and commonly used *ab initio* method for phonon calculations.[62,63] To avoid instabilities in phonon dispersion,[64] a relatively large supercell, a stricter convergence criterion of 10^{-8} eV, and a 24 × 12 × 12 *k*-point grid were employed.

3 Results and discussions

3.1 Crystal structure

Yamane *et al.*[38] reported that $Li_7P_3S_{11}$ contains PS_4^{3-} tetrahedra and P_2S_7 ditetrahedra, with Li ions interspersed between them.

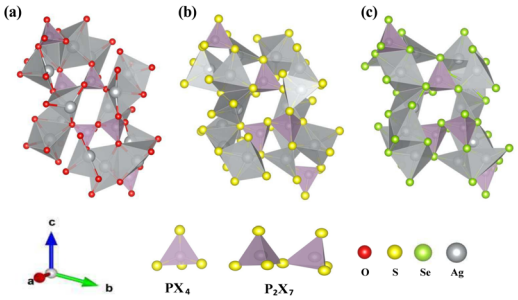

Fig. 1 The relaxed crystal structures of (a) $Ag_7P_3O_{11}$, (b) $Ag_7P_3S_{11}$, and (c) $Ag_7P_3Se_{11}$ are presented. These crystals each possess a triclinic structure and belong to the space group *P*1.

This crystal structure served as the foundation for structural relaxation calculations of $Ag_7P_3X_{11}$ (X = {O, S, and Se}), where lithium atoms were chemically replaced by silver, and sulfur by oxygen or selenium. The relaxed crystal structure of $Ag_7P_3X_{11}$ is depicted in Fig. 1, with the corresponding lattice parameters detailed in Table 1. The calculated structural parameters of $Ag_7P_3X_{11}$ closely approximate those of $Li_7P_3S_{11}$, and the space group remained unchanged after optimization. However, the unit-cell volume of $Ag_7P_3S_{11}$ is larger than that of $Li_7P_3S_{11}$ due to the greater ionic radius of Ag^+ (129 pm) compared to Li^+ (90 pm). The unit cell volume of $Ag_7P_3O_{11}$ is approximately 40% smaller than that of $Ag_7P_3S_{11}$, whereas the unit cell of $Ag_7P_3Se_{11}$ is about 12% larger than $Ag_7P_3S_{11}$. These volume differences are significantly influenced by the varying radii of the anions.

3.2 Electronic properties

To investigate the intrinsic redox stability of the $Ag_7P_3X_{11}$ compounds, the electronic band structure and density of states (DOS) were calculated using the HSE06 functional, as shown in Fig. 2. The bandgap of the material sets an upper limit on its electrochemical window[65] and affects the self-discharge rate of electrochemical devices, with a narrower bandgap leading to increased rates. According to the results in Table 2, the studied materials exhibit semiconducting behavior, with the S-substituted $Ag_7P_3S_{11}$ materials demonstrating a larger bandgap than the O/Se-substituted $Ag_7P_3X_{11}$ (X = {O, Se}), suggesting greater intrinsic redox stability for the S-substituted compounds. Furthermore, the DOS results indicate that the conduction band minimum (CBM) and valence band maximum (VBM), regardless of anion chemistry, are dominated by anion states.

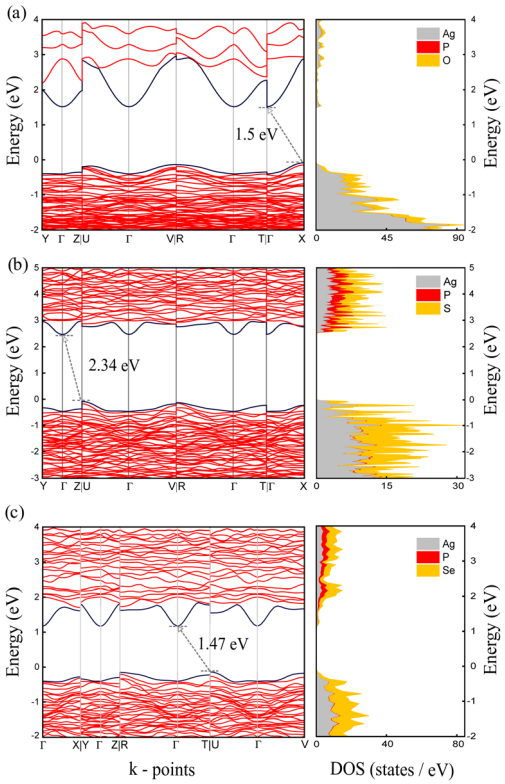

Fig. 2 Calculated electronic band structures and densities of states for (a) $Ag_7P_3O_{11}$, (b) $Ag_7P_3S_{11}$, and (c) $Ag_7P_3Se_{11}$ based on the HSE06 hybrid functional.

Table 2 The diffusion energy barrier and bandgap energy of studied materials

Composition	Energy bandgap (eV)	Small pathway energy barrier (eV)	Large pathway energy barrier (eV)
$Ag_7P_3O_{11}$	1.5	—	—
$Ag_7P_3S_{11}$	2.34	0.45	1.99
$Ag_7P_3Se_{11}$	1.47	1	2.22

The variation in electronic bandgaps for $Ag_7P_3O_{11}$ and $Ag_7P_3Se_{11}$ is minimal, likely due to the competitive formation of bonds between the anions O/S (where O is a harder base than Se) with Ag (a soft acid) and P (a hard acid), which stabilize the electronic structure. In contrast, $Ag_7P_3S_{11}$, which experiences a balanced competition for bond formation, exhibits a distinct electronic configuration and energy bandgap. The order of

Table 1 The calculated crystal structural parameters for $Li_7P_3S_{11}$ and $Ag_7P_3X_{11}$ (X = {O, S and Se}) are presented. The experimentally measured parameters for $Li_7P_3S_{11}$ as reported by Yamane *et al.* (2007)[38] are included in parentheses for comparison

Composition	*a* (Å)	*b* (Å)	*c* (Å)	*α* (deg)	*β* (deg)	*γ* (deg)	Volume (Å^3)	Anion radius (pm)
$Li_7P_3S_{11}$	6.18 (6.03)	12.12 (12.53)	12.41 (12.50)	107.54 (113.30)	102.65 (102.85)	102.22 (74.47)	827.58 (829.35)	—
$Ag_7P_3O_{11}$	5.70	10.80	11.20	108.12	101.36	100.99	619.69	126 (O^{2-})
$Ag_7P_3S_{11}$	6.28	12.21	12.77	109.13	99.86	101.46	878.47	170 (S^{2-})
$Ag_7P_3Se_{11}$	6.72	13.16	13.76	109.31	102.56	99.36	1085.14	184 (Se^{2-})

chemical bond energies ($Ag_7P_3O_{11}$ > $Ag_7P_3S_{11}$ > $Ag_7P_3Se_{11}$) can be understood in terms of stabilization from polarization and charge transfer.

Bader analysis of $Ag_7P_3Se_{11}$ reveals a lower electron density around Ag ions, as seen in Fig. 3a–c. This reduced electron density suggests weaker ionic bonding between Ag ions and their surrounding anions, facilitating easier movement of Ag ions and enhancing the ionic conductivity observed in $Ag_7P_3Se_{11}$. Fig. 3d–f shows the charge density difference isosurfaces for $Ag_7P_3X_{11}$. This charge density difference is calculated by subtracting the charge densities of individual components from that of the interacting system ($\rho_{Ag_7P_3X_{11}} - \rho_{Ag_7} - \rho_{P_3X_{11}}$). The analysis aligns with the Bader charge results, indicating smaller regions of electron accumulation around Se ions and reduced electron depletion around Ag ions in $Ag_7P_3Se_{11}$ compared to $Ag_7P_3S_{11}$ and $Ag_7P_3O_{11}$.

3.3 Phase stability

The thermal stabilities of $Ag_7P_3X_{11}$ were investigated through AIMD simulations. Fig. S1 (ESI)† confirms these materials are stable at room temperature. However, for $Ag_7P_3X_{11}$ (X = {O, Se}), bond breakages and notable structural distortions become apparent at extended simulation times. According to the hard and soft acids and bases (HSAB) theory,[66] these structures are prone to temperature-induced changes to maintain stability. The density of states of Γ-point phonons for $Ag_7P_3S_{11}$, depicted in Fig. 4, confirms the dynamical stability of this structure through the absence of negative frequencies in phonon dispersions.

A ternary phase diagram was constructed to investigate the phase stability of $Ag_7P_3X_{11}$, shown in Fig. 5. Compositional phase diagrams were established by selecting compounds from the Materials Project database.[67] Table S1 (ESI)† presents the equilibrium decomposition energies based on DFT-calculated energies. $Ag_7P_3O_{11}$ is found to be energetically stable against decomposition into binary and ternary compounds, whereas $Ag_7P_3S_{11}$ and $Ag_7P_3Se_{11}$ exhibit significantly lower stability in terms of energy changes. For more complex compositions, linear programming has been employed to accelerate materials screening and identify optimal decomposition pathways.[68]

Furthermore, the phase stability of $Ag_7P_3X_{11}$ was assessed by calculating its energy above the hull (E_{hull}), which indicates the compound's tendency for transformation into alternative phases. Temperature-dependent Gibbs free energy changes, incorporating vibrational entropy contributions, were utilized. The decomposition into a linear combination of stable phases $Ag_3PX_4 + Ag_4P_2X_7$ and $Ag_3PX_4 + P_2X_5$ were analyzed. $Ag_4P_2O_7$ and $Ag_4P_2Se_7$ exhibit remarkable stability at 0 K, whereas $Ag_4P_2S_7$

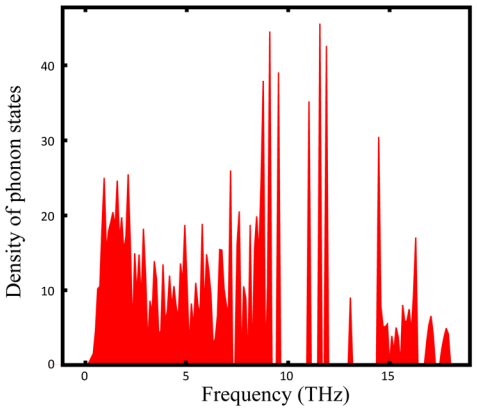

Fig. 4 Density of states of phonons for $Ag_7P_3S_{11}$.

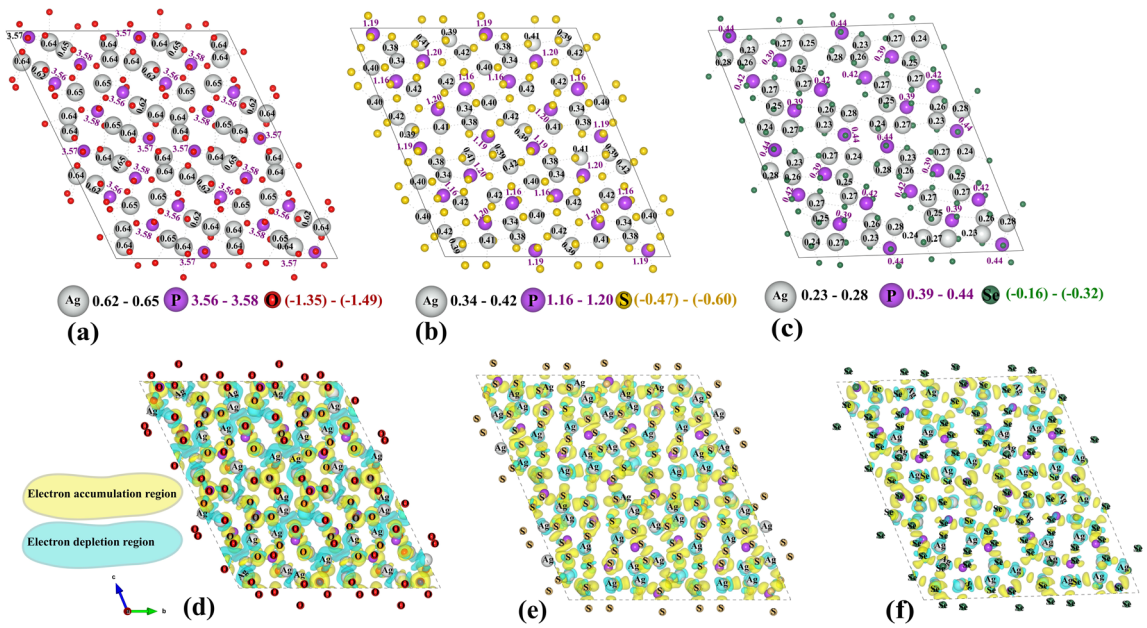

Fig. 3 The Bader charge distribution for Ag, P, O, S, and Se atoms in (a) $Ag_7P_3O_{11}$, (b) $Ag_7P_3S_{11}$, and (c) $Ag_7P_3Se_{11}$ is presented, with the charge ranges for each element indicated next to the respective symbol. Additionally, the charge density distributions for (d) $Ag_7P_3O_{11}$, (e) $Ag_7P_3S_{11}$, and (f) $Ag_7P_3Se_{11}$ are depicted, each with an isosurface level of 0.0041 e Å^{-3} for all three materials.

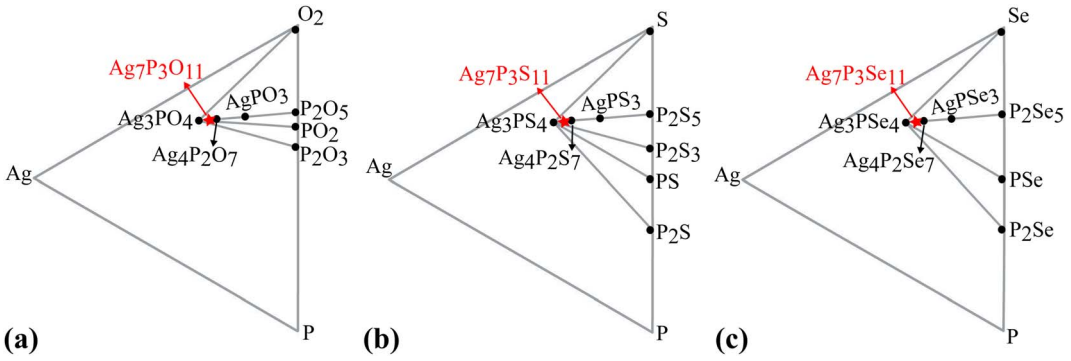

Fig. 5 Phase evolution of (a) $Ag_7P_3O_{11}$, (b) $Ag_7P_3S_{11}$, and (c) $Ag_7P_3Se_{11}$ is analyzed. For all compositions, the equilibrium state is determined by a combination of stable phases found within the linear and triangular surroundings of each composition. The position of each $Ag_7P_3X_{11}$ compound within this phase space is indicated by a red star.

appears metastable, potentially decomposing into Ag_3PS_4 + $Ag_4P_2S_7$ with an E_{hull} of 11.95 meV per atom. Subsequent examinations reveal that $Ag_7P_3O_{11}$ is stable, while $Ag_7P_3S_{11}$ and $Ag_7P_3Se_{11}$ are metastable, with E_{hull} values of 9.32 and 12.73 meV per atom, respectively, for decomposition into Ag_3PX_4 + P_2X_5. Decompositions result in the formation of passivation layers,[57] which play a crucial role in preventing further decomposition and expanding the electrochemical window.

Fig. 6 illustrates the temperature-dependent Gibbs free energy of $Ag_7P_3X_{11}$ for the predicted decomposition products. Considering decomposition products for each compound and the average ΔG values, one concludes that $Ag_7P_3O_{11}$ remains thermodynamically stable even at 1000 K. In contrast, $Ag_7P_3S_{11}$ exhibits a higher decomposition possibility, particularly towards lower-energy compounds Ag_3PS_4 + P_2S_5. Notably, the effect of phonon stabilization is most pronounced in $Ag_7P_3Se_{11}$. At temperatures exceeding 320 K, a phonon contribution larger than 12.73 meV per atom to the total free energy effectively stabilizes the phase of $Ag_7P_3Se_{11}$, preventing its decomposition into Ag_3PSe_4 + P_2Se_5.

The coordination number (CN) is a key metric used to quantify the number of neighboring atoms in compounds, providing valuable insights into structural and bonding characteristics. CN is calculated by integrating the first peak of the pair count distribution with the corresponding radii of the first nearest-neighbor bonds, denoted by r (Å).[69,70] Variations in CNs are indicative of transformations to new phases during ion transfer.[71,72] Notably, the pronounced peaks and larger bond radii of Se–Ag in $Ag_7P_3Se_{11}$, as illustrated in Fig. S2 (ESI)† and Table 3, suggest weaker bonds between Se atoms and Ag ions compared to those involving S and O atoms. This structural difference explains the higher conductivity observed in $Ag_7P_3Se_{11}$, detailed in Table 4. CN analyses reveal that O is more reactive towards Ag than S and Se, making the O–Ag pair more stable, which corroborates the enhanced stability of $Ag_7P_3O_{11}$, as discussed in Fig. 6. The fluctuations in CNs with temperature highlight the diversity in pair formation across the studied compounds, as seen in Fig. 7.

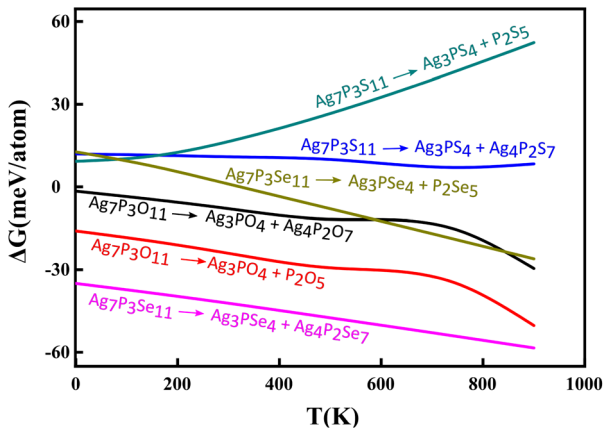

Fig. 6 The calculated temperature-dependent Gibbs free energy change for the reverse decomposition reaction of $Ag_7P_3X_{11}$.

3.4 Ionic diffusivity and conductivity

The primary reason for studying ion transport in SSEs is that ion conductivity is a crucial indicator of their performance. Understanding the ion transport mechanisms is essential for designing and optimizing SSEs with high conductivities. Ionic conductivity in crystalline materials is strongly influenced by crystal structure defects such as point defects, line defects, planar defects, volume defects, and electron defects.[73] The characteristics of superionic conductors are closely linked to their crystal structure, which naturally contains specific types of vacancies that facilitate ion movement.[33,74] Unlike conventional ionic solids where vacancies are typically generated by heating, these gaps are inherent to the material's crystal structure, a concept thoroughly explained by Geller *et al.*[75]

Fig. 9 illustrates the energy landscape for single Ag^+ ion migration across each channel, obtained through NEB calculations. It was determined that Ag^+ ion diffusion through vacancies between two pyrothiophosphate $P_2S_7^{4-}$ sites reduces lattice strain and significantly lowers the energy barrier. Notably, two PS_4 tetrahedra share one corner S atom. The migration energy barrier for Ag^+ ions depends on the density of vacancies in the lattice and the distance from the previous equilibrium position to the adjacent vacancy, enhancing diffusivity. AIMD simulations at 1200 K, sampled every 4 ps (total

Table 3 Distances between pairs, measured in angstroms (Å), are considered for the first nearest neighbors in the three studied compounds

r (Å)	$Ag_7P_3O_{11}$			$Ag_7P_3S_{11}$			$Ag_7P_3Se_{11}$		
Pairs	Ag–Ag	Ag–P	Ag–O	Ag–Ag	Ag–P	Ag–S	Ag–Ag	Ag–P	Ag–Se
600 K	2.70	3.35	2.25	3.05	3.35	2.45	3.15	3.45	2.75
750 K	2.72	3.25	2.20	3.00	3.40	2.50	3.10	3.50	2.65
900 K	2.75	3.15	2.25	2.95	3.45	2.65	3.05	3.55	2.70
1200 K	2.70	3.25	2.25	2.90	3.50	2.60	2.95	3.35	2.65

Table 4 The room temperature conductivity and activation energy for superionic conductors $Ag_7P_3X_{11}$ (X = {O, S, and Se}) are reported, along with corresponding values for $M_7P_3X_{11}$ (M = {Li, Na,} and X = {O, S, and Se}),[27] enclosed in parentheses

Composition	RT σ (mS cm^{-1})	Error bound [σ_{min}, σ_{max}]	RT E_a (eV)
$Li_7P_3O_{11}$	(0.03)	—	(0.38)
$Li_7P_3S_{11}$	(45.66)	—	(0.19)
$Li_7P_3Se_{11}$	(47.94)	—	(0.18)
$Na_7P_3O_{11}$	(0.003)	—	(0.53)
$Na_7P_3S_{11}$	(10.97)	—	(0.21)
$Na_7P_3Se_{11}$	(12.56)	—	(0.21)
$Ag_7P_3O_{11}$	0.03	[0.001, 0.199]	0.38 ± 0.06
$Ag_7P_3S_{11}$	1.21	[0.0003, 6.282]	0.27 ± 0.04
$Ag_7P_3Se_{11}$	13.98	[1.598, 33.113]	0.19 ± 0.03

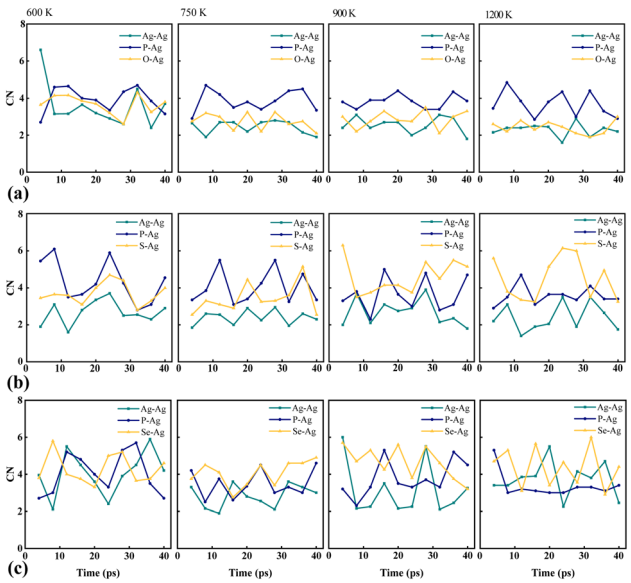

Fig. 7 Calculated average coordination numbers (CNs) for Ag as the central atom, with P, O, S, and Se as neighboring atoms, are presented for (a) $Ag_7P_3O_{11}$, (b) $Ag_7P_3S_{11}$, and (c) $Ag_7P_3Se_{11}$. These CNs illustrate the distribution of formation pairs involving Ag with each type of neighbor atom.

simulation time: 45 ps), confirm that ions preferentially utilize vacancies between $P_2X_7^{4-}$ and PX_4^{3-} sites for hopping, as shown in Fig. S3 (ESI).† Migration paths connecting two $P_2X_7^{4-}$ sites, either directly or *via* an intermediate PX_4^{3-}, were examined. The scenario where the Ag^+ ion moves between two closely spaced PX_4^{3-} tetrahedra, inducing significant lattice strain with a high energy barrier of about 30 eV for $Ag_7P_3S_{11}$, is detailed in Fig. S4 (ESI).†

Fig. 9a demonstrates that Ag^+ ions can diffuse easily through large pathways in $Ag_7P_3O_{11}$, involving hopping mechanisms. However, as shown in Fig. 9b, Ag^+ ions can be trapped in smaller pathways, potentially blocking these channels and altering the structure, potential energy surface, and migration barriers. Energy barriers for diffusion through both small and large pathways in $Ag_7P_3X_{11}$ (X = {S, Se}) are documented in Table 2. The shorter distances and intermediate PX_4^{3-} (X = {S, Se}) result in lower energy barriers.

To assess Ag^+ ion diffusivity in $Ag_7P_3X_{11}$ (X = {O, S, Se}) crystals, AIMD simulations were conducted at various temperatures (600 K, 750 K, 900 K, and 1200 K) without melting the crystal structure. The Arrhenius plots for the overall diffusion coefficient (eqn (1)) at these temperatures are depicted in Fig. 8. From the extrapolated room-temperature diffusion coefficients and eqn (3), the ionic conductivities were evaluated.

The diffusivities along various directions are quite similar due to the presence of empty active space facilitating hopping between two $P_2X_7^{4-}$ (X = {S and Se}) sites. The dominant transport channel is considered to be along the *a*–*b* direction, with diffusivities of 0.022 × 10^{-8}, 2.157 × 10^{-8}, and 29.541 ×

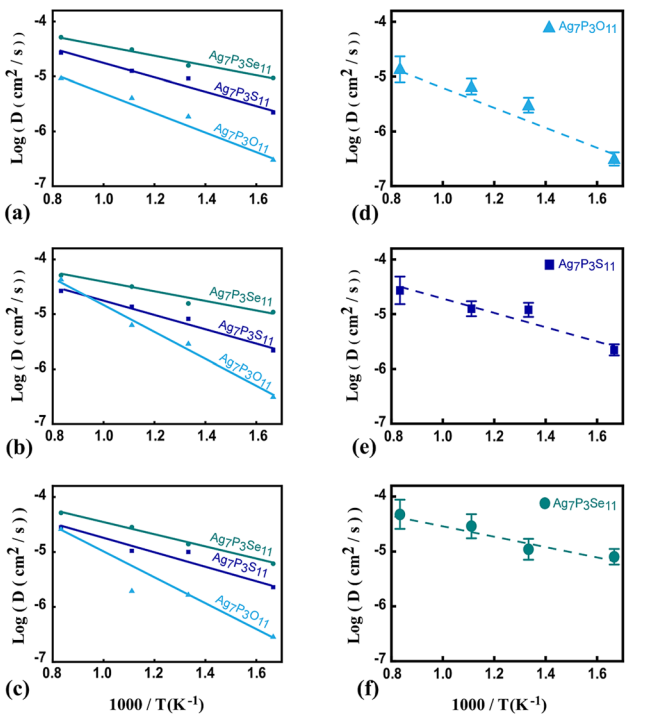

Fig. 8 The comparison of calculated ionic diffusivities for $Ag_7P_3X_{11}$ (X = {O, S, and Se}) across various temperatures (600 K, 750 K, 900 K, and 1200 K) includes (a) overall ionic diffusivity, (b) diffusivity in the *a*–*b* plane, and (c) diffusivity along the *c*-direction. A least-squares fit has been applied to the data to produce trend lines. Additionally, the Arrhenius plot of Ag^+ total diffusivities at these four temperatures for (d) $Ag_7P_3O_{11}$, (e) $Ag_7P_3S_{11}$, and (f) $Ag_7P_3Se_{11}$ includes error bars representing the statistical uncertainty of each data point.

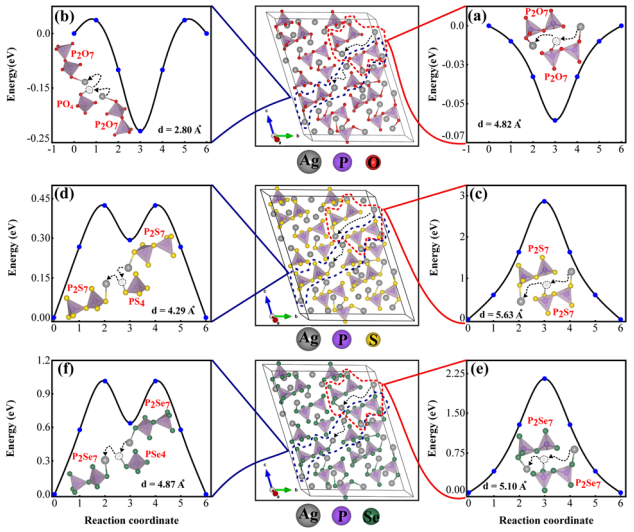

Fig. 9 The energy profiles illustrate the reaction paths of Ag^+ ion migration using the nudged elastic band (NEB) method. The diffusion barriers for Ag^+ ions at different distances were examined in (a) and (b) between two (P_2O_7) pyrophosphate units in $Ag_7P_3O_{11}$, (c) and (d) between two (P_2S_7) pyrothiophosphate units in $Ag_7P_3S_{11}$, and (e) and (f) between two (P_2Se_7) anions in $Ag_7P_3Se_{11}$.

10^{-8} ($cm^2\ s^{-1}$) for $Ag_7P_3O_{11}$, $Ag_7P_3S_{11}$, and $Ag_7P_3Se_{11}$ at room temperature, respectively, which are notably lower than those along the *c* direction (0.030×10^{-8}, 2.332×10^{-8}, and 37.995×10^{-8}) ($cm^2\ s^{-1}$). Although diffusion along the *c* direction is less facile than in the *a*–*b* directions, it still contributes to the overall diffusivity of the material (see Fig. 8). The extrapolated room-temperature conductivities and activation energies (eqn (4)) are summarized in Table 4. Specifically, the room-temperature conductivities and activation energies for $Ag_7P_3O_{11}$, $Ag_7P_3S_{11}$, and $Ag_7P_3Se_{11}$ are (0.03 ($mS\ cm^{-1}$) and 0.38 eV), (1.21 ($mS\ cm^{-1}$) and 0.27 eV), and (13.98 ($mS\ cm^{-1}$) and 0.19 eV), respectively. The extrapolated room temperature ionic conductivity increases as S is substituted by Se, even though the crystal structure remains unchanged through this replacement. The ionic diffusivity and conductivity of $Ag_7P_3Se_{11}$ are slightly larger than those of $Na_7P_3Se_{11}$, as reported by Wang *et al.*[27]

Two fundamental mechanisms for ion transport in SSEs are single-ion migration and concerted migrations involving multiple ions.[76] In single-ion migration, individual ions move between lattice sites through interconnected diffusion channels. Conversely, concerted migrations involve multiple ions simultaneously hopping to their nearest sites. While NEB calculations specifically focus on the single-ion migration, the conductivity results obtained from AIMD simulations are complementary to NEB analysis. By analyzing the dynamics of Ag^+ ions from AIMD simulations, it was concluded that the migration of most Ag ions occurs in a highly concerted fashion. This entails multiple ions simultaneously hopping into their nearest sites, suggesting a notable enhancement in the ionic conductivity of $Ag_7P_3Se_{11}$. The presence of high-energy sites and relatively flat energy landscapes play a critical role in activating concerted migration processes. The NEB calculations corroborated these observations, indicating that high-energy sites are associated with elongated spatial occupancy density of mobile Ag ions. The study further highlights that rapid diffusion in the examined super-ionic conductors does not primarily occur through isolated ion hopping, as commonly observed in solid materials.[76,77]

According to the HSAB theory[78] and Bader charge analysis, the bonding strength between the hard acid P and hard base O is larger than that with S and Se (P–O > P–S > P–Se). This observation indicates that, apart from anion substitutions, substitutions involving P have an impact on the diffusivity, conductivity, and stability of $Ag_7P_3X_{11}$.

4 Conclusions

This study utilized first-principles calculations to gain insights into ion diffusion mechanisms in solid-state electrolytes and to explore strategies for designing solid-state batteries with desirable chemical and physical properties. Bader analysis revealed a notable reduction in electron density around silver ions in $Ag_7P_3Se_{11}$, indicating weaker ionic bonds, which leads to increased mobility and elevated conductivity. Nudged elastic band (NEB) calculations investigated various diffusion pathways for $Ag_7P_3X_{11}$ (X = {O, S, and Se}) structures, concluding that the migration energy barrier for Ag ions depends on the density of vacancies in the lattice and the distance between the previous equilibrium position and the adjacent vacancy. Therefore, typical concerted migrations observed in AIMD simulations are the dominant diffusion mechanisms in $Ag_7P_3Se_{11}$. Among the studied structures, $Ag_7P_3Se_{11}$, with a higher number of vacant sites, exhibited the highest ionic conductivity of approximately 13.98 mS cm^{-1}.

Various calculations were also conducted to evaluate the stability of the studied materials. Phonon calculations based on density functional perturbation theory (DFPT) showed the absence of imaginary frequencies in the dispersions of $Ag_7P_3S_{11}$, confirming local stability. Thermal stability analysis based on AIMD simulations indicated that the materials are stable at room temperature, but as temperature increases, structural distortions occur along with the formation of new vacancies. Furthermore, phase stability analysis revealed that $Ag_7P_3S_{11}$ exhibits a greater tendency for decomposition, whereas $Ag_7P_3Se_{11}$ is metastable at lower temperatures but transitions to higher stability and enhanced resistance against decomposition beyond a certain temperature threshold. Finally, the RDF analysis showed strong peaks and larger bond radii of Se–Ag in $Ag_7P_3Se_{11}$, indicating weaker bonds between Se atoms and Ag ions, resulting in higher ionic conductivity in this material.

Author contributions

Amin Niksirat: conceptualization, methodology, formal analysis, investigation, data curation, writing-original draft, visualization. Maryam Soleimani: methodology, formal analysis, investigation, data curation, writing-original draft. Ali Lashani Zand: methodology, formal analysis, investigation. Mahdi Pourfath: conceptualization, resources, validation,

investigation, writing-original draft, writing-review & editing, supervision.

Conflicts of interest

There are no conflicts of interest to declare.

Acknowledgements

The authors acknowledge TU Wien Bibliothek for financial support through its Open Access Funding Programme.

Notes and references

1 Z. Xu, R. Chen and H. Zhu, *J. Mater. Chem. A*, 2019, **7**, 12645–12653.
2 G. Segev, J. Kibsgaard, C. Hahn, Z. J. Xu, T. G. Deutsch, C. Xiang, J. Z. Zhang, L. Hammarström, D. G. Nocera, A. Z. Weber, *et al.*, *J. Phys. D: Appl. Phys.*, 2022, **55**, 323003.
3 Z. Niazi, A. Hagfeldt and E. K. Goharshadi, *J. Mater. Chem. A*, 2023, **11**, 6659–6687.
4 X. Shen, H. Liu, X.-B. Cheng, C. Yan and J.-Q. Huang, *Energy Storage Mater.*, 2018, **12**, 161–175.
5 Q. Meng, J. Ma, Y. Zhang, Z. Li, C. Zhi, A. Hu and J. Fan, *Nanoscale*, 2018, **10**, 3385–3392.
6 S. Fleischmann, Y. Sun, N. C. Osti, R. Wang, E. Mamontov, D.-e. Jiang and V. Augustyn, *J. Mater. Chem. A*, 2020, **8**, 412–421.
7 Z. P. Cano, D. Banham, S. Ye, A. Hintennach, J. Lu, M. Fowler and Z. Chen, *Nat. Energy*, 2018, **3**, 279–289.
8 M. Forsyth, L. Porcarelli, X. Wang, N. Goujon and D. Mecerreyes, *Acc. Chem. Res.*, 2019, **52**, 686–694.
9 Q. Feng, X. Xie, B. Zheng and N. Liao, *ACS Appl. Energy Mater.*, 2023, **6**, 2698–2706.
10 J. C. Bachman, S. Muy, A. Grimaud, H.-H. Chang, N. Pour, S. F. Lux, O. Paschos, F. Maglia, S. Lupart, P. Lamp, *et al.*, *Chem. Rev.*, 2016, **116**, 140–162.
11 C. Li, Z.-y. Wang, Z.-j. He, Y.-j. Li, J. Mao, K.-h. Dai, C. Yan and J.-c. Zheng, *Sustainable Mater. Technol.*, 2021, **29**, e00297.
12 A. Manthiram, X. Yu and S. Wang, *Nat. Rev. Mater.*, 2017, **2**, 1–16.
13 C. Sun, J. Liu, Y. Gong, D. P. Wilkinson and J. Zhang, *Nano Energy*, 2017, **33**, 363–386.
14 Y. Zheng, Y. Yao, J. Ou, M. Li, D. Luo, H. Dou, Z. Li, K. Amine, A. Yu and Z. Chen, *Chem. Soc. Rev.*, 2020, **49**, 8790–8839.
15 Y.-Y. Sun, Q. Zhang, L. Yan, T.-B. Wang and P.-Y. Hou, *Chem. Eng. J.*, 2022, 135179.
16 E. Ilina, E. Lyalin, M. Vlasov, A. Kabanov, K. Okhotnikov, E. Sherstobitova and M. Zobel, *ACS Appl. Energy Mater.*, 2022, **5**, 2959–2967.
17 N. Vallana, E. Carena, N. Ceribelli, L. Mezzomo, G. Di Liberto, M. Mauri, C. Ferrara, R. Lorenzi, L. Giordano and R. Ruffo, *ACS Appl. Energy Mater.*, 2024, **7**, 1606–1617.
18 X. Feng, H. Fang, N. Wu, P. Liu, P. Jena, J. Nanda and D. Mitlin, *Joule*, 2022, **6**, 543–587.
19 N. Kamaya, K. Homma, Y. Yamakawa, M. Hirayama, R. Kanno, M. Yonemura, T. Kamiyama, Y. Kato, S. Hama and K. Kawamoto, *Nat. Mater.*, 2011, **10**, 682–686.
20 X. Yao, D. Liu, C. Wang, P. Long, G. Peng, Y.-S. Hu, H. Li, L. Chen and X. Xu, *Nano Lett.*, 2016, **16**, 7148–7154.
21 R. Murugan, V. Thangadurai and W. Weppner, *Angew. Chem., Int. Ed.*, 2007, **46**, 7778–7781.
22 R. Jalem, Y. Yamamoto, H. Shiiba, M. Nakayama, H. Munakata, T. Kasuga and K. Kanamura, *Chem. Mater.*, 2013, **25**, 425–430.
23 W. D. Richards, Y. Wang, L. J. Miara, J. C. Kim and G. Ceder, *Energy Environ. Sci.*, 2016, **9**, 3272–3278.
24 M. V. Reddy, C. M. Julien, A. Mauger and K. Zaghib, *Nanomaterials*, 2020, **10**, 1606.
25 A. Mauger, C. M. Julien, A. Paolella, M. Armand and K. Zaghib, *Materials*, 2019, **12**, 3892.
26 A. Miura, N. C. Rosero-Navarro, A. Sakuda, K. Tadanaga, N. H. Phuc, A. Matsuda, N. Machida, A. Hayashi and M. Tatsumisago, *Nat. Rev. Chem*, 2019, **3**, 189–198.
27 Y. Wang, W. D. Richards, S.-H. Bo, L. J. Miara and G. Ceder, *Chem. Mater.*, 2017, **29**, 7475–7482.
28 S. Banerjee, M. L. H. Chandrappa and S. P. Ong, *ACS Appl. Energy Mater.*, 2022, **5**, 35–41.
29 M. H. Morcali, *ChemistrySelect*, 2019, **4**, 9011–9017.
30 K. Braam and V. Subramanian, *Adv. Mater.*, 2015, **27**, 689–694.
31 Q. Yin, L. Chen, Y. Chen and F. Zhan, *Compos. Commun.*, 2021, **26**, 100728.
32 D. W. Kim, I.-S. Cho, S. Lee, S.-T. Bae, S. S. Shin, G. S. Han, H. S. Jung and K. S. Hong, *J. Am. Ceram. Soc.*, 2010, **93**, 3867–3872.
33 D. Chang, K. Oh, S. J. Kim and K. Kang, *Chem. Mater.*, 2018, **30**, 8764–8770.
34 G. Kresse and J. Furthmüller, *Phys. Rev. B: Condens. Matter Mater. Phys.*, 1996, **54**, 11169.
35 P. E. Blöchl, *Phys. Rev. B: Condens. Matter Mater. Phys.*, 1994, **50**, 17953.
36 J. P. Perdew, K. Burke and M. Ernzerhof, *Phys. Rev. Lett.*, 1996, **77**, 3865.
37 J.-H. Li and Y.-X. Yu, *Nanoscale*, 2021, **13**, 20637–20648.
38 H. Yamane, M. Shibata, Y. Shimane, T. Junke, Y. Seino, S. Adams, K. Minami, A. Hayashi and M. Tatsumisago, *Solid State Ionics*, 2007, **178**, 1163–1167.
39 T. H. Wan and F. Ciucci, *ACS Appl. Energy Mater.*, 2021, **4**, 7930–7941.
40 T. Wu, K. Zhu, C. Qin and K. Huang, *J. Mater. Chem. A*, 2019, **7**, 5612–5620.
41 P. Khakbaz, M. Moshayedi, S. Hajian, M. Soleimani, B. B. Narakathu, B. J. Bazuin, M. Pourfath and M. Z. Atashbar, *J. Phys. Chem. C*, 2019, **123**, 29794–29803.
42 G. Henkelman and H. Jónsson, *J. Chem. Phys.*, 2000, **113**, 9978–9985.
43 H. Wang, G. Zhao, S. Wang, D. Liu, Z. Mei, Q. An, J. Jiang and H. Guo, *Nanoscale*, 2022, **14**, 823–832.
44 C. Guan, Y. Yang, R. Ouyang, H. Jing, J. Yan and H. Zhu, *J. Mater. Chem. A*, 2023, **11**, 6157–6167.

45 Z. Yang, Y. Zheng, W. Li and J. Zhang, *Nanoscale*, 2021, **13**, 11534–11543.
46 C. Wang, K. Aoyagi and T. Mueller, *J. Mater. Chem. A*, 2021, **9**, 23206–23213.
47 Y. Wang, M. Wang, Z. Lu, D. Ma and Y. Jia, *Nanoscale*, 2021, **13**, 13390–13400.
48 W. G. Hoover, *Phys. Rev. A: At., Mol., Opt. Phys.*, 1985, **31**, 1695.
49 D. Frenkel and B. Smit, *Understanding Molecular Simulation: From Algorithms to Applications*, Elsevier, 2001, vol. 1.
50 N. Shuichi, *Prog. Theor. Phys. Suppl.*, 1991, **103**, 1–46.
51 S. Nosé, *Mol. Phys.*, 1984, **52**, 255–268.
52 H. Chun, K. Nam, S. J. Hong, J. Kang and B. Han, *J. Mater. Chem. A*, 2021, **9**, 15605–15612.
53 A. Marcolongo and N. Marzari, *Phys. Rev. Mater.*, 2017, **1**, 025402.
54 X. He, Y. Zhu, A. Epstein and Y. Mo, *npj Comput. Mater.*, 2018, **4**, 18.
55 N. J. de Klerk, E. van der Maas and M. Wagemaker, *ACS Appl. Energy Mater.*, 2018, **1**, 3230–3242.
56 L. Shcherbak, O. Kopach, P. Fochuk, A. Bolotnikov and R. James, *J. Phase Equilib. Diffus.*, 2015, **36**, 99–109.
57 Y. Mo, S. P. Ong and G. Ceder, *Chem. Mater.*, 2012, **24**, 15–17.
58 Y. Huang, Y. Yu, H. Xu, X. Zhang, Z. Wang and G. Shao, *J. Mater. Chem. A*, 2021, **9**, 14969–14976.
59 H. Huang, H.-H. Wu, C. Chi, J. Zhu, B. Huang and T.-Y. Zhang, *Nanoscale*, 2019, **11**, 18758–18768.
60 N. J. De Klerk and M. Wagemaker, *Chem. Mater.*, 2016, **28**, 3122–3130.
61 *I. C. S. Database, Inorganic Crystal Structure Database*, 2010, **https://icsd.fiz-karlsruhe.de/icsd/**.
62 S. Baroni, S. De Gironcoli, A. Dal Corso and P. Giannozzi, *Rev. Mod. Phys.*, 2001, **73**, 515.
63 N. Li, Y. Li and J. Fan, *Nanoscale*, 2021, **13**, 7234–7243.
64 I. Ansaripour and M. Pourfath, *J. Phys. Chem. C*, 2021, **125**, 15000–15011.
65 S. P. Ong, O. Andreussi, Y. Wu, N. Marzari and G. Ceder, *Chem. Mater.*, 2011, **23**, 2979–2986.
66 M. Saito, S. Kawaharasaki, K. Ito, S. Yamada, K. Hayamizu and S. Seki, *RSC Adv.*, 2017, **7**, 14528–14535.
67 A. Jain, S. P. Ong, G. Hautier, W. Chen, W. D. Richards, S. Dacek, S. Cholia, D. Gunter, D. Skinner, G. Ceder and K. A. Persson, *APL Mater.*, 2013, **1**, 011002.
68 X. Chen, C. Wang, Z. Li, Z. Hou and W.-J. Yin, *Sci. China Mater.*, 2020, 1024–1035.
69 C.-Y. Chou and G. S. Hwang, *Chem. Mater.*, 2013, **25**, 3435–3440.
70 A. L. Zand, A. Niksirat, Z. Sanaee and M. Pourfath, *ACS Omega*, 2023, **8**, 44698–44707.
71 S. Lee, M. Ko, S. C. Jung and Y.-K. Han, *ACS Appl. Mater. Interfaces*, 2020, **12**, 55746–55755.
72 M. K. Chan, C. Wolverton and J. P. Greeley, *J. Am. Chem. Soc.*, 2012, **134**, 14362–14374.
73 B. Zhang, R. Tan, L. Yang, J. Zheng, K. Zhang, S. Mo, Z. Lin and F. Pan, *Energy Storage Mater.*, 2018, **10**, 139–159.
74 M. Khalifa, S. El-Mashri and M. Avasthi, *Phys. B*, 2002, **321**, 388–392.
75 S. t. Geller and M. Lind, *J. Chem. Phys.*, 1970, **52**, 5854–5861.
76 X. He, Y. Zhu and Y. Mo, *Nat. Commun.*, 2017, **8**, 15893.
77 C. Wang, J. Liang, J. T. Kim and X. Sun, *Sci. Adv.*, 2022, **8**, eadc9516.
78 S. Balijapelly, Q. Zhang, P. Sandineni, A. Adhikary, S. Mohapatra, S. Sundaramoorthy, N. Gerasimchuck, A. V. Chernatynskiy and A. Choudhury, *ACS Appl. Energy Mater.*, 2021, **4**, 7942–7951.